Crystallization-Induced Microdomain Coalescence in Sphere-Forming Crystalline−Amorphous Diblock Copolymer Systems: Neat Diblock versus the Corresponding Blends

Yen-Yu Huang,[†] Ching Hua Yang,[†] Hsin-Lung Chen,*[,†] Fang-Choyu Chiu,[‡] Tsang-Lang Lin,[§] and Willisa Liou[⊥]

Department of Chemical Engineering, National Tsing Hua University, Hsin-Chu, Taiwan 30013, R.O.C.; Department of Chemical and Materials Engineering, Chang Gung University, Kwei-San, Taoyuan 333, Taiwan, R.O.C.; Department of Engineering and System Science, National Tsing Hua University, Hsin-Chu, Taiwan 30013, R.O.C.; and Department of Anatomy, Chang Gung University, Kwei-San, Taoyuan 333, Taiwan, R.O.C.

Received August 7, 2003; Revised Manuscript Received October 30, 2003

ABSTRACT: Crystallization in the microdomains of crystalline−amorphous diblock copolymers may induce domain coalescence when the crystallization temperature lies above the T_g of the amorphous matrix. In this study, the perturbation of microdomain structure driven by isothermal crystallization and postannealing in a poly(ethylene oxide)-*block*-poly(1,4-butadiene) (PEO-*b*-PB) and PEO-*b*-PB/PB homopolymer (h-PB) blends consisting of spherical PEO domains in the melt state is systematically investigated to reveal whether the presence of homopolymer in the amorphous matrix would hinder or facilitate the microdomain coalescence driven by the crystallization. Three samples with nearly the same volume fraction and length of PEO block are adopted for the study; the first is an asymmetric PEO-*b*-PB that contains no h-PB, the second is a blend containing 12 wt % of h-PB, and the third is a blend consisting of 63 wt % of h-PB. Characterization of the domain structure after isothermal crystallization and postannealing treatment by SAXS and TEM indicates that the blend containing the higher h-PB content exhibits the stronger resistance against microdomain coalescence. The resistance is proposed to stem from the diffusion barrier associated with the rejection of a portion of h-PB originally dissolved in the coronal regions of the micelles during the coalescence process.

Introduction

Molecular self-assembly in diblock copolymer and its blend with the corresponding homopolymer can generate a series of long-range ordered microdomains depending upon the segregation strength and the composition of the constituting components. The classical structures include lamellae, cylinder, and sphere, and complex structures such as the gyroid phase have also been disclosed.[1] These domain structures provide convenient templates for studying the phase transition of chain molecules under different degrees of spatial confinement. Crystalline−amorphous (C−A) diblock copolymer, as one of the most important instances, has been adopted as a template to explore the crystallization behavior of polymer chains confined in nanoscaled space once C block forms microdomains in the melt state.[2−8]

Confined crystallization in C-*b*-A has been subjected to a number of studies.[2−18] Microdomain geometry, strength of interblock repulsion, and the glass transition temperature of the amorphous matrix (T_g^A) have been considered as the major parameters that control the extent of confinement to the crystallization process. When T_c lies below T_g^A, the confinement is the strongest since the amorphous matrix remains rigid throughout the crystallization process. Such an effect is called "hard confinement".[19] In the case where the amorphous matrix is soft at T_c (i.e., $T_c \geq T_g^A$), crystallization of C block may still be locally restricted, and the matrix is said to impose a "soft confinement" to the crystallization process.[19] Both hard and soft confinements have drastic impacts on the overall crystallization kinetics, where homogeneous nucleation starts to dominate the crystallization process when C blocks form highly isolated domains such as cylinders, spheres, and spherical vesicles because the microdomains outnumber the heterogeneous nuclei significantly.[2−6,8,20−23]

Crystallization in C−A diblocks also induces complex structural transformations at different length scales. For crystallization under hard confinement, the mesophase structure in the melt state is expected to be preserved; nevertheless, the local structure within the C domains including the crystallite dimension and the orientation and stacking of the crystallites can be affected by the spatial confinement.[24−27] Identifying the strategy for tuning such a fine structure is useful for constructing the nanostructures with two length scales (i.e., structure-within-structure), where the larger one is prescribed by the periodic structure of the block copolymer and the smaller one is associated with the ordered arrangement of the crystallites within the microdomains.[23]

In addition to the formation of local structures within the crystalline domains, the overall melt morphology may be perturbed by the crystallization when T_c lies above T_g^A.[4,21,28−32] Crystallization prefers to break out the melt structure and transforms it into a lamellar morphology consisting of alternating crystalline and

[†] Department of Chemical Engineering, National Tsing Hua University.
[‡] Department of Chemical and Materials Engineering, Chang Gung University.
[§] Department of Engineering and System Science, National Tsing Hua University.
[⊥] Department of Anatomy, Chang Gung University.
* To whom correspondence should be addressed. E-mail: hlchen@che.nthu.edu.tw.

10.1021/ma0351468 CCC: $27.50
Published on Web 12/17/2003

Table 1. Characteristics of the PEO-*b*-PB and PEO-*b*-PB/h-PB Blend under Study

sample designation	PEO-*b*-PB-based copolymer				1,4-addition PB				
	$M_{b,PEO}$[a]	$M_{b,PB}$[a]	M_w/M_n	f_{PEO}	M_n	M_w/M_n	overall f_{PEO}	wt fraction of h-PB	melt structure of PEO domain
B63	6000	5000	1.04	0.50	2730	1.04	0.17	0.63	sphere
B12	6000	20400	1.04	0.21	1000	1.04	0.17	0.12	sphere
N00	6800	26000	1.04	0.17			0.17	0.00	sphere

[a] The molecular weight values listed refer to the number-average molecular weights.

amorphous layers with large lateral dimensions. Such a structural transformation, however, could cause unfavorable perturbations in the interfacial tension and the conformational entropy of the coronal A block chains, so another force may emerge to resist the structural transformation. The interplay among the driving force of crystallization and that stabilizing the melt mesophase and the activation barriers associated with the structural transformation may thus create the morphology intermediate to the melt mesophase and crystalline lamellar structure. For example, the spherical microdomains formed by polyethylene block in a polyethylene-*block*-poly(styrene-*r*-ethylene-*r*-butene) (E/SEB) were found to merge locally into disk- or rodlike crystalline domains upon the crystallization.[21] In a polystyrere-*block*-polybutadiene-*block*-poly(ϵ-caprolactone) (PS-*b*-PB-*b*-PCL) triblock copolymer, Balsamo et al. found that the core−shell cylinders consisting of PCL block as core and PB block as shell in the PS matrix deformed into the corresponding core−shell polygonal cylinders upon PCL block crystallization.[33] We have revealed the deformation of the spherical microdomains consisting of poly(ethylene oxide) (PEO) blocks in a PEO-*block*-polybutadiene (PEO-*b*-PB)/PB homopolymer (h-PB) blend into ellipsoid-like objects upon the crystallization of PEO.[32] Subsequent prolonged annealing of the crystalline sample near the onset of melting induced coalescence of the crystalline ellipsoids into a highly elongated prolate or a rodlike domain.[34] Such a postannealing-induced domain coalescence was distinguished from the microdomain coalescence which occurred in situ of the crystallization because the block chains in the microdomains remained crystalline during the postannealing while in the latter the block chains in the otherwise molten domains had large mobility to participate in the diffusion or conformational rearrangement necessary for creating the domain coalescence.

It is known that a specific microdomain morphology of C blocks can be obtained by the proper adjustment of the relative lengths of A and C blocks in neat C-*b*-A or by the uniform mixing of h−A with A blocks in C-*b*-A/h−A blend.[3,4,6,7] Although both approaches can yield identical microdomain morphology at a given overall volume fraction of A or C in the melt state, the extent of structural perturbation induced by the subsequent crystallization of C blocks may be different in that the blend consists of hompolymer chains. Whether the presence of homopolymer in the matrix would hinder or facilitate the microdomain coalescence associated with the crystallization is unknown. In this study, we intend to resolve this problem by examining the perturbation of spherical microdomain structure induced by crystallization in PEO-*b*-PB and its blend with h-PB. Three samples with nearly the same PEO block length and volume fraction of PEO (f_{PEO}) are adopted for the study; the first is a neat asymmetric PEO-*b*-PB that contains no h-PB, the second is a blend containing a small amount of h-PB (i.e., the system described in the previous paragraph), and the third is a blend consisting of the highest h-PB content. These samples are subjected to isothermal crystallizations and postannealing treatment, and small-angle X-ray scattering (SAXS) and transmission electron microscopy (TEM) are utilized to probe the resultant microdomain structures. It will be demonstrated that the presence of h-PB actually tends to hinder the microdomain coalescence induced by crystallization or postannealing.

Experimental Section

Materials and Sample Preparation. All the polymer samples used were purchased from Polymer Source, Inc. The symmetric PEO-*b*-PB with $M_{b,PEO} = 6000$ and $M_{b,PB} = 5000$ was used to blend with the h-PB with $M_{h-PB} = 2730$ to yield the diblock blend with $f_{PEO} = 0.17$. The weight fraction of h-PB in the sample was 0.63. This blend system was hence denoted by B63. The asymmetric PEO-*b*-PB with $M_{b,PEO} = 6000$ and $M_{b,PB} = 20\,400$ was used to blend with the h-PB with $M_{h-PB} = 1000$. The f_{PEO} of the blend was also 0.17, and the weight fraction of h-PB in the PB matrix was 0.12. This blend was thus designated as B12. It should be noted that the molecular weights of the h-PB samples were always lower than those of the corresponding PB blocks, i.e., $\alpha = M_{h,PB}/M_{b,PB} < 1$; in this case, the wet-brush blends with h-PB uniformly solubilized in the coronal regions of the spherical micelles were expected to be formed.[35−37] The molecular weights of PEO and PB blocks in the highly asymmetric PEO-*b*-PB were $M_{b,PEO} = 6800$ and $M_{b,PB} = 26\,000$, which prescribed a f_{PEO} of 0.17. This diblock was used without adding any h-PB and was denoted by N00. Table 1 summarizes the characteristics of the three systems studied here.

Microphase-separated blends (B63 and B12) were prepared by solution mixing using toluene as the solvent, followed by removing the solvent in vacuo at 80 °C. The PEO microdomains in the melt state were spheres in all samples studied.

The amorphous samples used for SAXS characterization were prepared by first annealing at 80 °C ($T_m^{PEO} < 80$ °C < T_{ODT}; $T_{ODT} > 150$ °C) for 5 min followed by cooling to room temperature. It should be noted that although T_m^{PEO} was higher than room temperature, the crystallinity developed (through heterogeneous nucleation) upon cooling to room temperature was effectively undetectable by DSC because the crystallization within the predominant fraction of PEO spherical domains had to proceed through homogeneous nucleation which occurred at very deep undercooling (≥90 K).[3,4] In this case, the morphology of the cooled sample should correctly represent the melt morphology of the system.

The isothermal crystallization was conducted by quenching directly from 80 °C to T_c followed by crystallization at T_c for 10 h to reach the saturated crystallinity. Some of the as-crystallized samples were subjected to the postannealing treatment. The annealing was conducted by storing the as-crystallized samples in an oven equilibrated at $T_a = 38$ °C for 96 h.

SAXS Measurement. All SAXS experiments were conducted at room temperature (ca. 27 °C). The X-ray source of SAXS, an 18 kW rotating anode X-ray generator (Rigaku) equipped with a rotating anode Cu target, was operated at 200 mA and 40 kV. The incident X-ray beam was monochromated by a pyrolytic graphite, and a set of three pinhole inherent collimators were used so that the smearing effects inherent in slit-collimated small-angle X-ray cameras can be avoided. The scattered intensity was detected by a two-

dimensional position-sensitive detector (ORDELA model 2201X, Oak Ridge Detector Laboratory Inc.) with 256 × 256 channels (active area 20 × 20 cm^2 with ~1 mm resolution). All data were corrected by the background (dark current and empty beam scattering) and the sensitivity of each pixel of the area detector. The area scattering pattern has been radially averaged to increase the photon counting efficiency compared with one-dimensional linear detector. The intensity profile was output as the plot of the scattering intensity (I) vs the scattering vector, $q = 4\pi/\lambda \sin(\theta/2)$ (θ = scattering angle).

TEM Experiment. The real-space morphology of the blends was observed by a JEM-2000EX II transmission electron microscope operated at 100 kV. The film specimens were microtomed at −95 °C using a Reichert Ultracut E low-temperature sectioning system. The ultrathin sections were picked onto the copper grids coated with carbon-supporting films followed by staining by exposure to the vapor of 2% osmium tetraoxide (OsO_4) solution for 2 h. It should be noted that the originally amorphous samples may undergo crystallization during the ultrathin section preparation at −90 °C; therefore, for the morphological observations of the amorphous samples, the ultrathin sections were annealed at 65 °C for 3 min to melt the PEO crystals prior to OsO_4 staining. OsO_4 is a preferential staining agent for PB blocks, so the PB matrix appears dark in the TEM micrographs.

Results and Discussion

We will present the results in the decreasing order of the h-PB content in the sample; namely, the result of B63 blend will be presented first followed by that of B12 and then N00 system. The effect of h-PB on the perturbation of the domain structure will be disclosed by comparing the results of these three systems.

Microdomain Structure in B63 Blend. This system contains the highest h-PB content, where the homopolymer accounts for 63% of the total sample weight. Figure 1 shows a series of SAXS profiles of B63 blend subjected to isothermal crystallization at T_c's ranging from −50 to −23 °C. The scattering curve of the amorphous sample is also displayed for comparison. The broad maxima denoted by "$i = n$" ($n = 1, 2$) are the form factor peaks associated with the scattering from isolated microdomains.[4,32,38] The form factor scattering depends on the geometric characteristics of the domains, including the shape, the average dimension, and the dimension distribution;[39] therefore, analysis of the observed form factor profiles is useful for evaluating the perturbation of domain structure induced by the crystallization.

The form factor peaks are seen to broaden and shift after the crystallization, indicating that the structure of the original molten domains has been perturbed upon crystallization. Figure 2 shows the position of the first-order form factor as a function of T_c. The form factor peak moves toward lower q with increasing T_c. Using the peak position of the amorphous sample as the reference, two regimes split by the vertical line are identified in Figure 2. The form factor peak locates at slightly higher q than that of the amorphous sample for T_c lower than −31 °C (denoted by regime I), while it situates at lower q for T_c lying above −31 °C (regime II). Shift of the form factor maxima to higher q upon crystallization has also been found for B12 blend studied previously;[32] similar to that system, the observed peak shift cannot be simply attributed to volume contraction of spherical microdomains after crystallization because the radii obtained from the fits using the spherical form factor yield the domain density that is higher than the crystal density of PEO. The observed form factor profiles can be alternatively fitted by the ellipsoidal form factor,

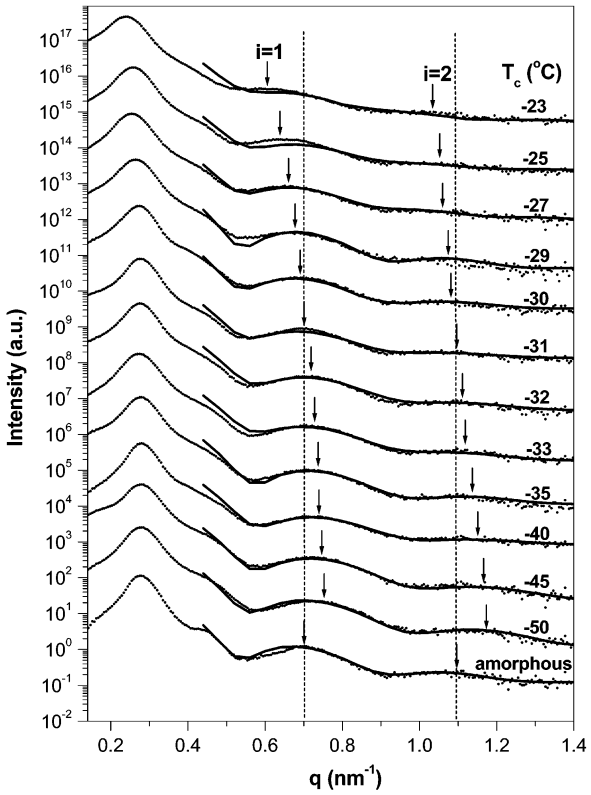

Figure 1. Room temperature SAXS profiles of B63 blend collected after crystallization at T_c ranging from −50 to −23 °C. The intensity profile of the amorphous sample is also displayed for comparison. In the plot, the maxima marked by "$i = n$" ($n = 1, 2$) are the form factor peaks associated with the scattering from isolated microdomains. The solid curves are the profiles calculated using ellipsoidal form factor. The dimensions of the ellipsoidal domains obtained from the form factor fits are listed in Table 2.

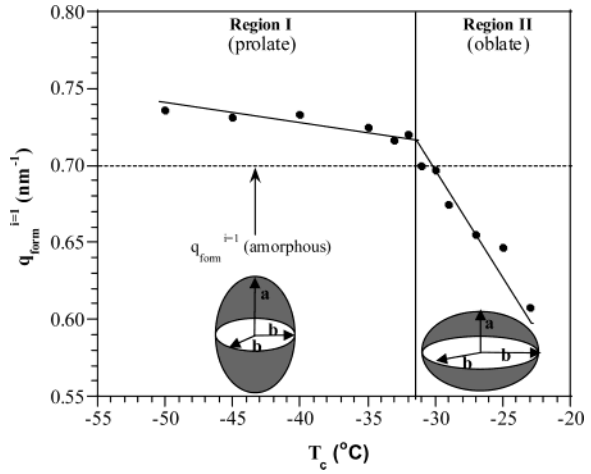

Figure 2. Position of the first-order form factor peak ($q_{form}^{i=1}$) of B63 blend as a function of T_c. The horizontal dash line specifies the $q_{form}^{i=1}$ of the amorphous sample. Two regimes separated by the vertical line are identified. The form factor peak locates at slightly higher q than that of the amorphous sample for T_c lower than −31 °C (regime I), while the form factor maxima situate at lower q for T_c lying above −31 °C (regime II).

which yields reasonable density for the crystalline domains.[32] The average dimensions of the ellipsoidal domains, $\langle a \rangle$ and $\langle b \rangle$ (with the axis of a being the rotating axis of the ellipse), deduced from the fit are listed in Table 2. It can be seen that crystallization

Table 2. Results of the Fits by the Ellipsoidal Form Factor for Isothermally Crystallized B63 Blend

T_c (°C)	$\langle a \rangle$ (nm)	$\langle b \rangle$ (nm)	σ_a[a] (nm)	σ_b[a] (nm)	aspect ratio ($\langle a \rangle / \langle b \rangle$)
−23	6.3	9.5	0.5	0.1	0.66
−25	6.5	9.2	0.2	0.2	0.71
−27	6.8	9.4	0.1	0.2	0.72
−29	7.3	9.0	0.2	0.3	0.81
−30	7.7	8.7	0.5	0.8	0.89
−31	8.1	8.0	0.7	1.0	1.01
−32	7.9	7.8	0.7	1.0	1.01
−33	8.4	7.5	0.4	0.1	1.12
−35	8.9	7.5	0.7	0.5	1.19
−40	9.0	7.3	0.7	0.5	1.23
−45	9.5	7.3	0.2	0.4	1.30
−50	10.0	7.5	0.4	0.2	1.33
b	8.4	8.3	0.8	0.8	1.01

[a] σ_a and σ_b are the standard deviations of *a* and *b*, respectively, with the assumption of Gaussian distribution. [b] Amorphous.

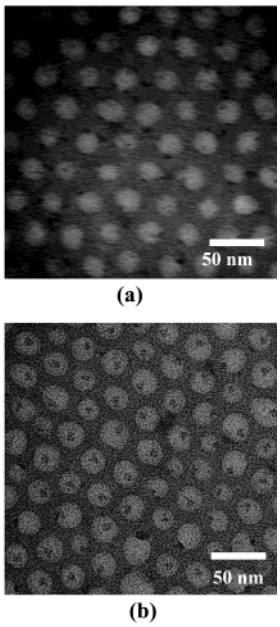

Figure 3. TEM micrographs of B63 blend after crystallization at (a) −23 °C and (b) −50 °C.

below −31 °C slightly deforms the original molten sphere with radius of 8.4 nm into ellipsoid-like domain with the aspect ratio $\langle a \rangle / \langle b \rangle > 1$ due to the formation of anisotropic lamellar crystallite in the domain. The ellipsoidal object with $a > b$ is also known as prolate (as schematically illustrated in Figure 2).

The form factor peaks situate at lower *q* than those of the amorphous sample in regime II ($T_c > -31$ °C). Because volume expansion of the individual spherical domains is not expected upon the crystallization, such a form factor shift seems to imply the coalescence of the PEO spheres. To testify whether such a domain coalescence occurs, the TEM experiment was conducted to reveal the real-space domain structure in the as-crystallized samples. Figure 3 displays the representative TEM micrographs of the samples crystallized at −23 and −50 °C. The difference between the images of the PEO domains in these two samples is very subtle, where the domains in the sample crystallized at −23 °C are not obviously larger. This demonstrates that microdomain coalescence did not take place for crystallization above −31 °C. As a matter of fact, the observed form factor profiles in regime II can also be fitted by the ellipsoidal form factor under the constraint that the

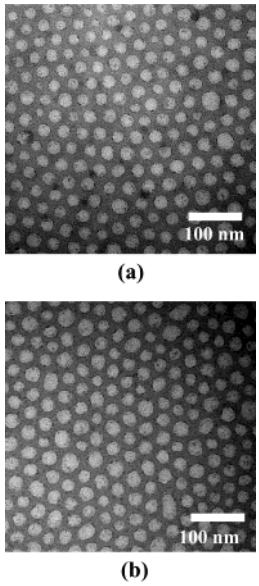

Figure 4. TEM micrographs of B63 blend having been postannealed at 38 °C. The samples had been crystallized at (a) −23 and (b) −50 °C prior to the postannealing.

microdomain volume retains (or slightly decreases) after the crystallization. The calculated profiles are shown by the solid curves in Figure 1, and the average dimensions of the ellipsoids obtained from the fits are tabulated in Table 2. In contrast to the case of $T_c < -31$ °C, $\langle b \rangle$ is now greater than $\langle a \rangle$, i.e., the aspect ratio < 1. This type of ellipsoid is called oblate (as schematically illustrated in Figure 2).

The form factor analysis suggests that the PEO spherical microdomains in the melt state were perturbed subtly upon the crystallization. The spherical domains deformed into prolate objects upon crystallization below −30 °C, whereas they transformed into oblate domains when T_c lay above −30 °C. No domain coalescence was observed over the T_c range studied. The origin of the transition between prolate and oblate domains with respect to T_c is not clear at the current stage. The difference in domain geometry may stem from the different shape of the lamellar crystallites formed within the PEO domains. The crystallite in the prolate domain might be rodlike in shape, whereas that in the oblate domain is more or less disklike in shape.

The effect of postannealing on the structure of the crystalline domains in B63 is also evaluated here. In this experiment, the as-crystallized samples were annealed for 96 h at 38 °C, which situated closely to the onset of melting of the as-crystallized samples. Such a postannealing treatment was found to induce the coalescence of two or three crystalline domains into a highly elongated prolate or rodlike domain in B12 blend, presumably due to the increase of crystallinity that further deformed the crystalline domains.[34] Figure 4 shows the TEM micrographs of the annealed B63 blends which were initially crystallized at −23 and −50 °C. It is clear that the postannealing treatment does not induce coalescence of the crystalline microdomains.

Microdomain Structure in B12 Blend. This system only contains 12 wt % of h-PB, and the perturbations of microdomain structure induced by isothermal crystallization and postannealing had been reported previously.[32,34] The SAXS form factor peaks of the as-crystallized B12 blend were located at higher *q* than those of the amorphous counterpart irrespective of T_c.

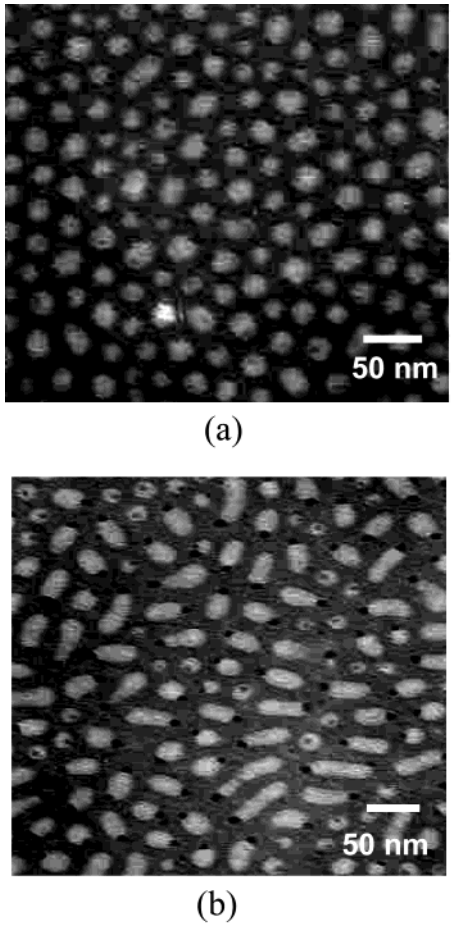

Figure 5. TEM micrographs of B12 blend: (a) as-crystallized at −30 °C and (b) annealed at 38 °C after crystallization at −30 °C.

There was no systematic variation of the form factor position with T_c. Analysis of the observed form factor profiles by the ellipsoidal form factor indicated that original molten spheres with radius of ca. 9.4 nm deformed into prolate domains with the aspect ratio $\langle a \rangle / \langle b \rangle \approx 1.3$ irrespective of T_c. Approximately two or three prolate domains welded into one rodlike domains upon postannealing near the onset of melting point, as demonstrated by the representative TEM micrographs in Figure 5 showing the morphology of crystalline PEO domains before and after the annealing.

Microdomain Structure in N00 System. The main difference between N00 and the foregoing blend systems is the lack of h-PB in N00. Figure 6 exhibits a series of SAXS profiles of N00 isothermally crystallized at three T_c's. The amorphous sample displays a broad primary peak associated with the interdomain correlation at $q = 0.2$ nm^{-1}, signifying that the PEO spherical domains in the melt state do not pack into the macrolattice found in the low-molecular-weight blends.[38] The form factor maxima are seen to shift slightly to higher q after the crystallization irrespective of T_c, signaling perturbation of microdomain geometry.

The real-space morphology of the as-crystallized N00 is presented by the TEM micrographs in Figure 7. The spherical domains in the amorphous sample do not exhibit apparent long-range order, consistent with the SAXS result. The lack of long-range order may be due to the fast solvent removal in the solvent casting process and the slow dynamics associated with the rearrangement of microdomains into the equilibrium lattice

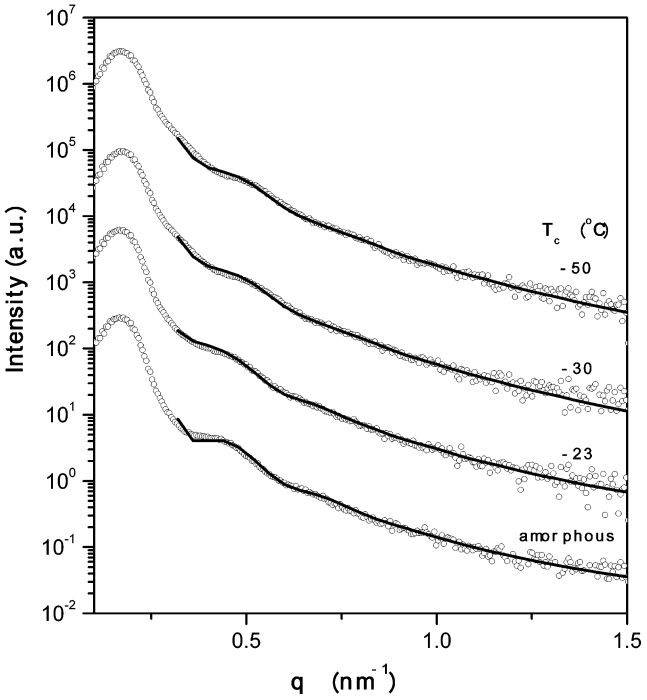

Figure 6. Room temperature SAXS profiles of N00 collected after crystallization at −23, −30, and −50 °C. The intensity profile of the amorphous sample is also displayed for comparison. The solid curves are the profiles calculated using ellipsoidal form factor fitting. The dimensions of the ellipsoidal domains obtained from the form factor fits are listed in Table 3.

because of long PB block length. In contrast to the blend systems, the microdomain geometry in the melt state is obviously perturbed by the isothermal crystallization, where highly elongated prolate or rodlike domains are identified in the as-crystallized sample irrespective of T_c. These rods are of ca. 40−80 nm in length and ca. 28 nm in diameter with no preferred orientation. The image resembling that of individual spheres or ellipsoids with diameter of ca. 22 nm is also observed in small proportion. Such an image could be due to the projection of the crystalline domains that remain uncoalescenced or that of the rodlike domains aligning side-on in the thin section. Since the volume of the individual rods exceeds that of a single microdomain found in the amorphous sample, the rodlike domains must have been formed through coalescence of the spherical domains in the crystallization process, where approximately two to four domains weld into one rod.

We also try to fit the form factor profiles in Figure 6 by the prolate form factor using the average dimensions estimated from the TEM micrographs as the initial guesses. The fitted profiles are plotted as the solid curves in Figure 6, and the dimensions of the prolates derived from the fits are tabulated in Table 3. It can be seen that the prolate form factor fits the experimental data well, and the domain dimensions derived from the fit agree with that estimated from the TEM micrographs.

Figure 8 presents the TEM micrographs of the post-annealed N00 having been subjected to isothermal crystallization at −23 and −50 °C. It can be seen that the dimensions of the rodlike domains do not change obviously upon the annealing.

The results presented have shown that under given volume fraction and length of PEO block the perturba-

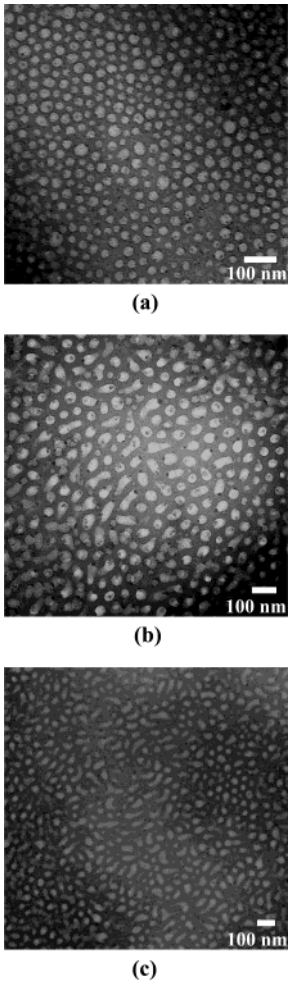

Figure 7. TEM micrographs of N00 in (a) amorphous state and the as-crystallized state with T_c = (b) −23 and (c) −50 °C.

Table 3. Results of the Fits by Ellipsoidal Form Factor for Isothermally Crystallized N00 System

T_c (°C)	$\langle a \rangle$ (nm)	$\langle b \rangle$ (nm)	σ_a[a] (nm)	σ_b[a] (nm)	aspect ratio ($\langle a \rangle / \langle b \rangle$)
−23	25.0	12.0	1.5	1.5	2.08
−30	30.0	11.0	1.3	1.2	2.73
−50	30.0	11.0	1.3	1.2	2.73
b	13.0	12.0	2.0	2.0	1.08

[a] σ_a and σ_b are the standard deviations of *a* and *b*, respectively, with the assumption of Gaussian distribution. [b] Amorphous.

tion of the domain structure is affected by the content of h-PB in the system. The blend containing the highest h-PB content, i.e., B63 blend, exhibits the strongest resistance against the structural perturbation, where neither crystallization nor postannealing can induce the microdomain coalescence. The microdomain remained isolated after isothermal crystallization in B12 system, but domain coalescence occurred as the as-crystallized sample was subjected to a postannealing treatment. In the neat PEO-*b*-PB the microdomain coalescence was already prevalent during the isothermal crystallization. Therefore, the homopolymer solubilized in the coronal regions of the spherical micelles (consisting of PEO domain and the coronal PB blocks) in the melt tends to resist the microdomain coalescence driven by crystallization or postannealing.

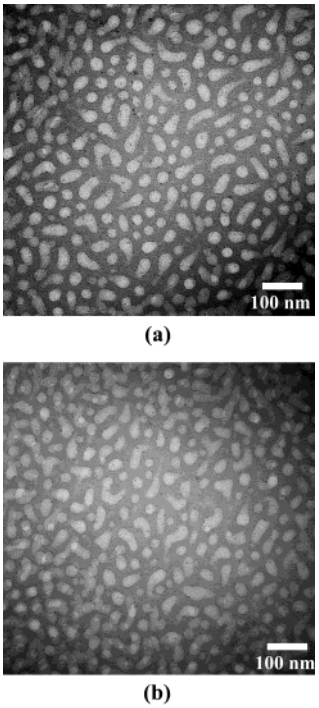

Figure 8. TEM micrographs of N00 having been postannealed at 38 °C. The samples had been crystallized at (a) −23 and (b) −50 °C prior to the postannealing.

In the crystallization process, the original spherical domains deform into ellipsoid-like objects due to the formation of lamellar crystallites within the domains. Such a deformation leads to an increase in interfacial energy since the spherical microdomains in the melt state have the lowest surface-to-volume ratio. Because the composition studied here (f_{PEO} = 0.17) lies in the vicinity to that corresponding to the cylindrical−spherical domain transition, a moderate perturbation in interfacial curvature may be sufficient to bring about domain coalescence to reduce the interfacial energy.[34] Nevertheless, the domain coalescence in the blend requires a portion of the h-PB chains dissolved in the coronal regions of the micelles to be pulled out, which results in a loss of entropy of mixing. An entropic force hence exists to resist the domain welding, and such a force will be the strongest in B63 blend because the coalescence process involves the rejection of the most h-PB content among the systems studied. On the other hand, the diffusion barrier associated with the rejection of h-PB chains out of the coronal regions could also be the main contribution to the resistance.

A preliminary calculation is conducted here to examine whether the gain in free energy of mixing could outweigh the reduction in interfacial energy so as to prohibit the domain coalescence in B63 blend. According to the theory of block copolymer/homopolymer blend by Leibler and Pincus, the free energy of mixing between the coronal A blocks and homopolymer A per micelle is given by[40]

$$F_{mix} = k_B T p \delta \left(\frac{\eta}{1-\eta} \right) \ln \eta \qquad (1)$$

where p is the association number of the micelle, $\delta = M_{b,A}/M_{h,A}$, and η is the fraction of the homopolymer in the coronal region. For B63 blend, p = 289, δ = 2.0, and η = 0.79 if all h-PB is solubilized in the micelle

Table 4. Elliptic Surface Area (S), Amount of h-PB Remaining in the Coronal Regions (η), Free Energy of Mixing (F_{mix}), and Interfacial Free Energy (F_{int}) before and after Coalescence of Two Ellipsoidal Domains for B63 Blend Calculated Using the Domain Dimensions in Table 2

	before coalescence					after coalescence				
T_c (°C)	S (nm^2)	η	F_{mix} ($\times 10^{18}$) (J)	F_{int} ($\times 10^{18}$) (J)	F ($\times 10^{18}$)[a] (J)	S (nm^2)	η	F_{mix} ($\times 10^{18}$) (J)	F_{int} ($\times 10^{18}$) (J)	F ($\times 10^{18}$)[a] (J)
−23	1780.14	0.79	−3.24	4.62	1.38	1387.6	0.69	−3.02	3.60	0.58
−25	1725.72	0.79	−3.21	4.46	1.25	1366.3	0.71	−3.04	3.53	0.49
−27	1824.70	0.79	−3.19	4.70	1.51	1452.9	0.71	−3.00	3.74	0.74
−29	1784.82	0.79	−3.16	4.58	1.42	1459.5	0.70	−2.97	3.75	0.78
−30	1758.32	0.79	−3.15	4.51	1.36	1465.6	0.71	−2.97	3.76	0.79
−31	1621.92	0.79	−3.14	4.15	1.01	1389.4	0.71	−2.96	3.55	0.59
−32	1542.16	0.79	−3.12	3.94	0.82	1321.2	0.71	−2.95	3.37	0.42
−33	1528.08	0.79	−3.11	3.90	0.79	1333.7	0.71	−2.95	3.40	0.45
−35	1592.62	0.79	−3.08	4.05	0.97	1404.0	0.72	−2.93	3.57	0.64
−40	1551.54	0.79	−3.02	3.90	0.88	1376.4	0.72	−2.87	3.46	0.59
−45	1615.34	0.79	−2.95	4.03	1.08	1445.3	0.72	−2.81	3.60	0.79
−50	1736.68	0.79	−2.89	4.29	1.40	1559.6	0.73	−2.75	3.85	1.10

[a] $F = F_{mix} + F_{int}$.

corona. The corresponding interfacial free energy is given by[41,42]

$$F_{int} = S\left[\frac{k_B T}{a^2}\left(\frac{\chi_{AB}}{6}\right)^{1/2}\right] \quad (2)$$

where S is the surface area of the microdomain, a is the Kuhn length ($a = 0.45$ nm for PEO), and χ_{AB} is the Flory−Huggins interaction parameter where $\chi_{AB} = -0.0185 + 39.476/T$ for PEO-*b*-PB as determined by SAXS.[43]

Assuming that h-PB in the as-crystallized samples remains completely solubilized in the coronal regions and that the degree of stretching of PB blocks (or the coronal shell thickness) is unperturbed, it is straightforward to calculate the volume fraction of the coronal shell of the micelle after microdomain coalescence. The amount of h-PB remaining in the coronal regions (i.e., η) and hence F_{mix} after the domain coalescence can then be obtained. Using the dimensions of the ellipsoidal domains in Table 2, we have calculated F_{mix} and F_{int} at various T_c's for the case where two as-crystallized ellipsoidal domains merge along a axis to yield a prolate with the dimensions of $2\langle a\rangle$ and $\langle b\rangle$. Table 4 compares the sum of these two free energies, $F = F_{mix} + F_{int}$, before and after the coalescence. It can be seen that F is indeed reduced after the coalescence because the reduction of F_{int} is always more significant than the gain in F_{mix}. This suggests that the gain in free energy of mixing is not the major contribution to the resistance toward microdomain coalescence in B63 blend. Instead, the diffusion barrier associated with the rejection of the h-PB chains out of the coronal regions could be responsible for the resistance.

On basis of the results presented here, it is concluded that C-*b*-A/h−A blend tends to exert a stronger confinement effect toward crystallization than the corresponding C-*b*-A; consequently, diblock copolymer blend may be considered as a favorable template for studying the crystallization of polymers under soft confinement.

Conclusions

The extent of structural perturbation induced by isothermal crystallization and postannealing in sphere-forming PEO-*b*-PB and PEO-*b*-PB/h-PB blends has been studied to reveal the effect of the presence of h-PB on the extent of structural perturbation. Addition of h-PB into the system was found to hinder the coalescence of the microdomains. B63 blend displayed the strongest resistance against the domain coalsecence, where neither crystallization nor postannealing could induce the microdomain coalescence. The microdomain coalescence occurred upon postannealing in B12 blend, whereas isothermal crystallization only resulted in domain deformation. Microdomain coalescence has already occurred during the isothermal crystallization in N00. The resistance toward domain coalescence exerted by h-PB in B63 blend was proposed to stem from the diffusion barrier associated with the rejection of a portion of h-PB out of the coronal regions of the micelles, while the corresponding gain in free energy of mixing was minor compared with the reduction in interfacial free energy upon domain coalescence.

Acknowledgment. This work was supported by the National Science Council of R.O.C. under Grant NSC-92-2216-E-007-032.

References and Notes

(1) Hamley, I. W. *The Physics of Block Copolymers*; Oxford University Press: New York, 1998.
(2) Weimann, P. A.; Hajduk, D. A.; Chu, C.; Chaffin, K. A.; Brodil, J. C.; Bates, F. S. *J. Polym. Sci., Part B: Polym. Phys.* **1999**, *37*, 2053.
(3) Chen, H.-L.; Hsiao, S.-C.; Lin, T.-L.; Yamauchi, K.; Hasegawa, H.; Hashimoto, T. *Macromolecules* **2001**, *34*, 671.
(4) Chen, H.-L.; Wu, J.-C.; Lin, T.-L.; Lin, J. S. *Macromolecules* **2001**, *34*, 6936.
(5) Loo, Y.-L.; Register, R. A.; Ryan, A. J.; Dee, G. T. *Macromolecules* **2001**, *34*, 8968.
(6) Xu, J.-T.; Turner, S. C.; Fairclough, J. P. A.; Mai, S.-M.; Ryan, A. J.; Chainbundit, C.; Booth, C. *Macromolecules* **2002**, *35*, 3614.
(7) Xu, J.-T.; Fairclough, J. P. A.; Mai, S.-M.; Ryan, A. J.; Chainbundit, C. *Macromolecules* **2002**, *35*, 6937.
(8) Lee, W.; Chen, H.-L.; Lin, T.-L. *J. Polym. Sci., Part B: Polym. Phys.* **2002**, *40*, 519.
(9) Douzinas, K. C.; Cohen, R. E. *Macromolecules* **1992**, *25*, 5030.
(10) Cohen, R. E.; Bellare, A.; Drzewinski, M. A. *Macromolecules* **1994**, *27*, 2321.
(11) Hamley, I. W.; Fairclough, J. P. A.; Ryan, A. J.; Bates, F. S.; Towns-Andrews, E. *Polymer* **1996**, *37*, 4425.
(12) Cohen, R. E.; Cheng, P. L.; Douzinas, K.; Kofinas, P.; Berney, C. V. *Macromolecules* **1990**, *23*, 324.
(13) Nojima, S.; Kikuchi, N.; Rohadi, A.; Tanimoto, S.; Sasaki, S. *Macromolecules* **1999**, *32*, 3727.
(14) Schnablegger, H.; Rein, D. H.; Rempp, P.; Cohen, R. E. *J. Polym. Eng.* **1996**, *16*, 1.
(15) Lotz, B.; Kovacs, A. J. *ACS Polym. Prepr* **1969**, *10*, 820.
(16) Zhu, L.; Huang, P.; Chen, W. Y.; Ge, Q.; Quirk, R. P.; Cheng, S. Z. D.; Thomas, E. L.; Lotz, B.; Hsiao, B. S.; Yeh, F.; Liu, L. *Macromolecules* **2002**, *35*, 3553.

(17) Zhu, L.; Cheng, S. Z. D.; Calhoun, B. H.; Ge, Q.; Quirk, R. P.; Thomas, E. L.; Hsiao, B. S.; Yeh, F.; Lotz, B. *Polymer* **2001**, *42*, 5829.
(18) Zhu, L.; Chen, Y.; Zhang, A.; Calhoun, B. H.; Chun, M.; Quirk, R. P.; Cheng, S. Z. D.; Hsiao, B. S.; Yeh, F.; Hashimoto, T. *Phys. Rev. B* **1999**, *60*, 10022.
(19) Zhu, L.; Mimnaugh, B. R.; Ge, Q.; Quirk, R. P.; Cheng, S. Z. D.; Thomas, E. L.; Lotz, B.; Hsiao, B. S.; Yeh, F.; Liu, L. *Polymer* **2001**, *42*, 9121.
(20) Loo, Y.-L.; Register, R. A.; Ryan, A. J. *Phys. Rev. Lett.* **2000**, *84*, 4120.
(21) Loo, Y.-L.; Register, R. A.; Ryan, A. J. *Macromolecules* **2002**, *35*, 2365.
(22) Muller, A. J.; Balsamo, V.; Arnal, M. L.; Jakob, T.; Schmalz, H.; Abetz, V. *Macromolecules* **2002**, *35*, 3048.
(23) Chen, H.-L.; Lin, S.-Y.; Huang, Y.-Y.; Chiu, F.-C.; Liou, W.; Lin, J. S. *Macromolecules* **2002**, *35*, 9434.
(24) Quiram, D. J.; Register, R. A.; Marchand, G. R.; Adamson, D. H. *Macromolecules* **1998**, *31*, 4891.
(25) Hamley, I. W.; Fairclough, J. P. A.; Terrill, N. J.; Ryan, A. J.; Lipic, P. M.; Bates, F. S.; Towns-Andrews, E. *Macromolecules* **1996**, *29*, 8835.
(26) Zhu, L.; Cheng, S. Z. D.; Calhoun, B. H.; Ge, Q.; Quirk, R. P.; Thomas, E. L.; Hsiao, B. S.; Yeh, F.; Lotz, B. *J. Am. Chem. Soc.* **2000**, *122*, 5957.
(27) Zhu, L.; Cheng, S. Z. D.; Huang, P.; Ge, Q.; Quirk, R. P.; Thomas, E. L.; Lotz, B.; Hsiao, B. S.; Yeh, F.; Liu, L. *Adv. Mater.* **2002**, *14*, 31.
(28) Nojima, S.; Kato, K.; Yamamoto, S.; Ashida, T. *Macromolecules* **1992**, *25*, 2237.
(29) Nojima, S.; Nkano, H.; Takahashi, Y.; Ashida, T. *Polymer* **1994**, *35*, 3479.
(30) Nojima, S.; Nkano, H.; Ashida, T. *Polymer* **1993**, *34*, 4168.
(31) Nojima, S.; Yamamoto, S.; Ashida, T. *Polym. J.* **1995**, *27*, 673.
(32) Chen, H.-L.; Li, H.-C.; Huang, Y.-Y.; Chiu, F.-C. *Macromolecules* **2002**, *35*, 2417.
(33) Balsamo, V.; von Gyldenfeldt, F.; Stadler, R. *Macromolecules* **1999**, *32*, 1226.
(34) Huang, Y.-Y.; Chen, H.-L.; Li, H.-C.; Lin, T.-L.; Lin, J. S. *Macromolecules* **2003**, *36*, 282.
(35) Winey, K. I.; Thomas, E. L.; Fetter, L. J. *Macromolecules* **1992**, *25*, 2645.
(36) Hashimoto, T.; Tanaka, H.; Hasegawa, H. *Macromolecules* **1990**, *23*, 4378.
(37) Tanaka, H.; Hasegawa, H.; Hashimoto, T. *Macromolecules* **1991**, *24*, 240.
(38) Huang, Y.-Y.; Chen, H.-L.; Hashimoto, T. *Macromolecules* **2003**, *36*, 764.
(39) Feigin, L. A.; Svergun, D. I. *Structure Analysis by Small-Angle X-ray and Neutron Scattering*; Plenum Press: New York, 1987.
(40) Leibler, L.; Pincus, P. A. *Macromolecules* **1984**, *17*, 2922.
(41) Helfand, E.; Sapse, A. M. *J. Chem. Phys.* **1975**, *62*, 1327.
(42) Helfand, E.; Tagami, Y. *J. Chem. Phys.* **1972**, *56*, 3592.
(43) Huang, Y.-Y. Ph.D. Thesis, National Tsing Hua University, 2004.

MA0351468